Ab initio magneto-optical properties of bcc Ni/Ni(100)

C. Etz,[1] A. Vernes,[1] L. Szunyogh,[1,2] and P. Weinberger[1]
[1]*Center for Computational Materials Science, Vienna University of Technology, Gumpendorferstrasse 1a, A-1060 Vienna, Austria*
[2]*Department of Theoretical Physics, Institute of Physics, Budapest University of Technology and Economics, Budafoki út 8, H-111 Budapest, Hungary*

(Received 21 November 2007; revised manuscript received 19 January 2008; published 19 February 2008)

The inter- and intralayer contributions to the layer-resolved complex optical conductivity tensor for semi-infinite layered systems are calculated in terms of the Luttinger formula within the spin-polarized relativistic screened Korringa-Kohn-Rostoker method. *Ab initio* Kerr angles are then obtained for arbitrary geometry and incidence via a 2×2 matrix technique including all multiple reflections and all optical interferences. Applied to in-plane single-domain magnetized bcc Ni/Ni(100), it is proven that the assumed appropriate formula of Kerr angles widely used to explain magneto-optical Kerr effect with rotating magnetic field measurements fully agrees with our *ab initio* Kerr data. From the experimental Kerr data of Tian *et al.* [Phys. Rev. Lett. **94**, 137210 (2005)], however, it cannot be concluded that the deduced magnetic properties apply for bulk Ni, since about 75% of the contributions to the Kerr rotation angle arise from the surface.

DOI: 10.1103/PhysRevB.77.064420 PACS number(s): 75.70.Rf, 78.20.Ls, 78.66.Bz

I. INTRODUCTION

The magnetic-optical Kerr effect with rotating magnetic field (ROTMOKE) technique as suggested by Mattheis and Quednau is a powerful experimental tool to determine the anisotropy field strength.[2] This experimental method is based on the longitudinal magneto-optical Kerr effect (MOKE) which occurs in a sufficiently large rotating magnetic field ensuring a single domain behavior of the ferromagnetic probe. Recently, ROTMOKE has been used to obtain the magnetocrystalline anisotropy of a bcc Ni thick film deposited on GaAs(001).[1] Because of this reference to the ROTMOKE deduced magnetocrystalline anisotropy constant ascribed to the bcc Ni bulk, the main challenge of the present paper is to clarify the role played by surface layers in ROTMOKE and to present a layer-resolved magnetocrystalline anisotropy (MCA) for bcc Ni/Ni(100). Since the interplay between MOKE and MCA was already discussed elsewhere,[3] the present comparison also serves as an indirect proof of the experimental expression in Ref. 2, which relates MCA to ROTMOKE.

Strictly speaking, the longitudinal MOKE configuration is valid within a ROTMOKE experiment only, when at least the average in-plane magnetization of the probe is in the plane of incidence. If this magnetization is perpendicular to the plane of incidence, a transverse geometry within the ROTMOKE applies. Thus, with the exception of these two particular cases, in a ROTMOKE measurement, in fact, one typically has an intermediate setup in between the longitudinal and transverse geometries. Exactly, this situation is addressed by our *ab initio* calculations, within which the direction of all layer-resolved in-plane magnetizations has been simultaneously varied from the transverse to the longitudinal configuration by keeping fixed the position of the incidence plane. Although a given arbitrary orientation of all in-plane layer-resolved magnetizations not necessarily corresponds to an overall equilibrium magnetic configuration of bcc Ni/Ni(100), this magnetic phase represents always a stable one in terms of density functional theory (DFT).[4]

The paper is organized as follows. The basic theoretical concepts used to calculate the inter- and intralayer contributions to the complex optical conductivity within the spin-polarized relativistic screened Korringa-Kohn-Rostoker method are briefly described in Sec. II A. Section II B contains a *modus operandi* to determine the Kerr angles by including all multiple reflections and optical interferences within a layered system via the so-called 2×2 matrix technique. Section III gives some details concerning the applied numerical schemes. For bcc Ni/Ni(100), the layer-resolved permittivities (Sec. IV A) together with the *ab initio* Kerr angles for oblique incidence (Secs. IV B and IV C) and the calculated magnetocrystalline anisotropy (Sec. IV D) are discussed at length in Sec. IV. Finally, Sec. V summarizes the main results.

II. THEORETICAL FRAMEWORK

A. Optical conductivity tensor

In 1957, Kubo developed a realistic response theory,[5] which provides a purely quantum statistical description of near-equilibrium irreversible processes. Since within Kubo's response theory one only needs to describe the initial quantum equilibrium state of the system, this kind of transport theory is well suited to be implemented within a first-principles method based on the DFT. In particular, this applies to the wave vector $\vec{q}$ and frequency ω dependent complex optical conductivity tensor as given by the well-known Kubo formula:[6]

$$\tilde{\sigma}_{\mu\nu}(\vec{q},\omega)=\beta\mathcal{L}\left[\langle J^{\mu}_{\vec{q}}(t);J^{\nu}_{-\vec{q}}\rangle_{\mathrm{eq}}\right]\big|_{-i\omega}\quad(\mu,\nu=x,y,z),\tag{1}$$

where

$$\mathcal{L}\left[g(y)\right]\big|_{x}=\int_{0}^{\infty}dy g(y)\exp(-xy),\quad x\in\mathbb{C}\tag{2}$$

is the Laplace transform of a function $g(y)$ satisfying the Dirichlet conditions, and $\beta=(k_BT)^{-1}$ is the so-called inverse

temperature, since only the canonical correlation $\langle \ldots \rangle_{\mathrm{eq}}$ of the electronic current density operator $\vec{J}$ components in the equilibrium state is required.

Here, Luttinger's formula will be applied[7]

$$\tilde{\sigma}_{\mu\nu}(\vec{q},\omega) = \frac{\tilde{\Sigma}_{\mu\nu}(\vec{q},\omega) - \tilde{\Sigma}_{\mu\nu}(\vec{q},0)}{\hbar\omega + i\delta}, \tag{3}$$

which is equivalent to Eq. (1) in a vector potential description of the electric field[8] and introduces a positive infinitesimal δ to get the Laplace transform (2) for a purely imaginary argument $-i\omega$ converged. In the current-current correlation function in Eq. (3),

$$\tilde{\Sigma}_{\mu\nu}(\vec{q},\omega) = \frac{i\hbar}{V}\sum_{m,n}\frac{f(\varepsilon_m) - f(\varepsilon_n)}{\varepsilon_m - \varepsilon_n + \hbar\omega + i\delta} J^{\mu}_{\vec{q},mn} J^{\nu}_{-\vec{q},nm}, \tag{4}$$

the factor δ can be viewed as a finite lifetime broadening, which accounts for all scattering processes at $T \neq 0$ that are commonly not incorporated in a standard DFT approach. Furthermore, because Eq. (1) leads to Eq. (3) if and only if the external electromagnetic field is never turned off,[8] $\delta > 0$ describes also the interaction of the system with its surroundings. Note that Eq. (4) yields $\tilde{\Sigma}_{\mu\nu}(\vec{q},\omega)$ in a representation, which diagonalizes the one-electron unperturbed Hamiltonian H_0, with $f(\varepsilon)$ being the Fermi-Dirac distribution function, ε_m and ε_n a pair of eigenvalues of H_0, $J^{\mu}_{\vec{q},mn}$ denoting the matrix elements of the current density operator $J^{\mu}_{\vec{q}}$, and V corresponds to the reference (crystalline) volume.

In order to calculate $\tilde{\Sigma}_{\mu\nu}(\vec{q},\omega)$ within the Korringa-Kohn-Rostoker method,[9] a contour integration technique in the complex energy plane at finite temperature can be used.[8,10] This technique exploits the properties of the Fermi-Dirac distribution function $f(z)$ of complex argument $z \in \mathbb{C}$ to select a contour Γ such that by using the residue theorem

$$\begin{aligned}\tilde{\Sigma}_{\mu\nu}(\vec{q},\omega) = {} & \oint_{\Gamma} dz f(z)\tilde{\Sigma}_{\mu\nu}(\vec{q};z+\hbar\omega+i\delta,z) \\ & - \left[\oint_{\Gamma} dz f(z)\tilde{\Sigma}_{\mu\nu}(-\vec{q};z-\hbar\omega+i\delta,z)\right]^{*} \\ & - 2i\delta_T \sum_{k=-N_2+1}^{N_1} [\tilde{\Sigma}_{\mu\nu}(\vec{q};z_k+\hbar\omega+i\delta,z_k) \\ & + \tilde{\Sigma}^{*}_{\mu\nu}(-\vec{q};z_k-\hbar\omega+i\delta,z_k)]\end{aligned} \tag{5}$$

and

$$\tilde{\Sigma}_{\mu\nu}(\vec{q},0) = \oint_{\Gamma} dz f(z)\tilde{\Sigma}_{\mu\nu}(\vec{q};z,z) - 2i\delta_T \sum_{k=-N_2+1}^{N_1} \tilde{\Sigma}_{\mu\nu}(\vec{q};z_k,z_k), \tag{6}$$

where the kernel $\tilde{\Sigma}_{\mu\nu}(\vec{q};z_1,z_2)$ can be written in terms of the resolvent $G(z)$ as

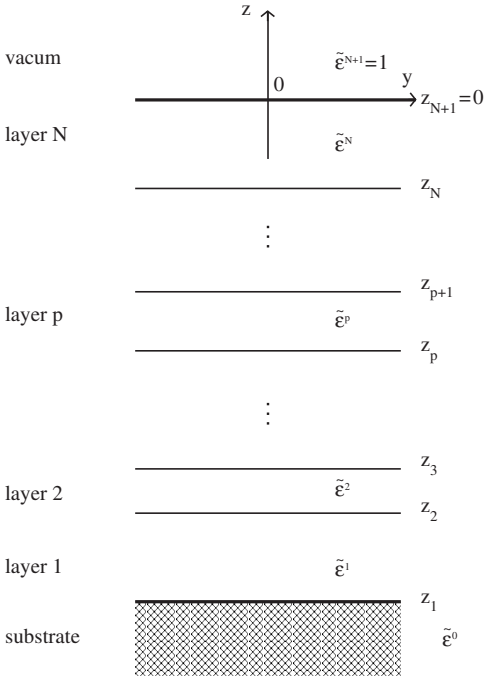

FIG. 1. The macroscopic model of a layered system used within the 2×2 matrix technique. Not shown here is the $0x$ axis perpendicular to the plane of the figure.

$$\tilde{\Sigma}_{\mu\nu}(\vec{q};z_1,z_2) = -\frac{\hbar}{2\pi V}\mathrm{Tr}[J^{\mu}_{\vec{q}}G(z_1)J^{\nu}_{-\vec{q}}G(z_2)]. \tag{7}$$

In Eqs. (5) and (6), N_1 (N_2) is the number of Matsubara poles $z_k = \varepsilon_F + i(2k-1)\delta_T$, with ε_F being the Fermi level, $k = 0, \pm 1, \pm 2, \ldots$, and $\delta_T = \pi k_B T$, in the upper (lower) semiplane included in Γ with the only constraint that $\delta > \delta_2$. Here, $\tilde{\Sigma}_{\mu\nu}(\vec{q};z_1,z_2)$ as given by Eq. (7) is calculated[11] by using the relativistic current density operator and the Green's function as directly obtained from the spin-polarized relativistic screened Korringa-Kohn-Rostoker (SKKR) method.[4]

Being interested in magneto-optics in the visible regime, where the leading interaction is the electric dipole one, the wave-vector dependence of the optical conductivity tensor is in the following neglected by simply setting $\vec{q}=0$.

B. 2×2 matrix technique

Since the pioneering work of Abelés in 1950,[12] there have been several methods known in the literature[13] which properly describe multiple reflections and interferences in layered system using, for example, a 4×4 matrix formalism.[14] In the present paper, the theoretical framework accounting for all possible reflections and optical interferences within a layered system consists of a 2×2 matrix technique previously developed in Ref. 15 based on Mansuripur's strategy.[16]

From an optical point of view, each layer p is assumed to be a homogeneous, linear, and anisotropic conducting medium (see Fig. 1) characterized by the complex permittivity tensor $\tilde{\boldsymbol{\varepsilon}}^{p}(\omega)$, which within the Gaussian system of units reads

$$\tilde{\boldsymbol{\varepsilon}}^{p}(\omega) = \boldsymbol{I} + \frac{4\pi i}{\tilde{\omega}} \tilde{\boldsymbol{\sigma}}^{p}(\omega), \tag{8}$$

where $\boldsymbol{I}$ is the 3×3 identity matrix and $\tilde{\omega}=\omega - i\delta$ is the complex frequency, with δ explained in Sec. II A. The layer-resolved optical conductivity $\tilde{\boldsymbol{\sigma}}^{p}(\omega)$, on the other hand, is directly obtained[17] from the inter- and intralayer contributions $\tilde{\boldsymbol{\sigma}}^{pq}(\omega)$,

$$\tilde{\boldsymbol{\sigma}}^{p}(\omega) = \sum_{q=1}^{N} \tilde{\boldsymbol{\sigma}}^{pq}(\omega) \quad (p = 1, \ldots, N). \tag{9}$$

Here and in the following, layers are numbered starting with the first ($p=1$) on top of a semi-infinite substrate, such that if N layers are considered, the index of the most upper (surface) layer is given by $p=N$. It is also convenient to label the substrate and the vacuum by 0 and $N+1$, respectively.

The normal modes of the electric and magnetic transverse plane waves propagating in a layer p are calculated by solving the Fresnel (characteristic) equation,[18]

$$|\tilde{n}_{p}^{2}\delta_{\mu\nu} - \tilde{n}_{p\mu}\tilde{n}_{p\nu} - \tilde{\varepsilon}_{\mu\nu}^{p}| = 0 \quad (\mu, \nu = x, y, z), \tag{10}$$

which is of fourth order in the z-Cartesian component $\tilde{n}_{pz}$ of the complex refraction vector. The other two Cartesian components,

$$\tilde{n}_{px} = -\sin\theta\cos\varphi = n_x,$$

$$\tilde{n}_{py} = -\sin\theta\sin\varphi = n_y \tag{11}$$

are all known in terms of the spherical colatitude θ ($0 \leqslant \theta \leqslant 90°$) and longitude φ ($0 \leqslant \varphi \leqslant 360°$) of the incident light coming in from the vacuum side. For each normal mode $\tilde{n}_{pz}^{(k)}$ ($k=1, \ldots, 4$), the Helmholtz equation[19]

$$\sum_{\nu=x,y,z} (\tilde{n}_{p}^{2}\delta_{\mu\nu} - \tilde{n}_{p\mu}\tilde{n}_{p\nu} - \tilde{\varepsilon}_{\mu\nu}^{p})\mathcal{E}_{p\nu} = 0 \quad (\mu = x, y, z) \tag{12}$$

then immediately provides the electric field $\vec{\mathcal{E}}_{p}^{(k)}$, which, in turn, when substituted into the curl Maxwell equation (Faraday's law),[20]

$$\vec{H}_{p} = \vec{n}_{p} \times \vec{E}_{p},$$

finally yields the magnetic field $\vec{\mathcal{H}}_{p}^{(k)}$.

In practice, however, the determination of $\vec{\mathcal{E}}_{p}^{(k)}$ is complicated by the fact that the Helmholtz equation (12) for a given $\tilde{n}_{pz}^{(k)}$ has to be solved by keeping at least one Cartesian component of the electric field arbitrary. Among all possible parametrization of the electric fields, a physically very transparent scheme results by following Mansuripur's strategy:[16]

$$\begin{cases} \mathcal{E}_{px}^{(k)} = \text{arbitrary} \\ \mathcal{E}_{py}^{(k)} = \tilde{\alpha}_{p}^{(k)}\mathcal{E}_{px}^{(k)} \\ \mathcal{E}_{pz}^{(k)} = \tilde{\beta}_{p}^{(k)}\mathcal{E}_{px}^{(k)} \end{cases} \quad \text{for } k = 1 \text{ and } 3 \tag{13}$$

and

$$\begin{cases} \mathcal{E}_{px}^{(k)} = \tilde{\alpha}_{p}^{(k)}\mathcal{E}_{py}^{(k)} \\ \mathcal{E}_{py}^{(k)} = \text{arbitrary} \\ \mathcal{E}_{pz}^{(k)} = \tilde{\beta}_{p}^{(k)}\mathcal{E}_{py}^{(k)} \end{cases} \quad \text{for } k = 2 \text{ and } 4. \tag{14}$$

Explicit expressions of the coefficients $\tilde{\alpha}_{p}^{(k)}$ and $\tilde{\beta}_{p}^{(k)}$ ($k=1, \ldots, 4$) in Eqs. (13) and (14) can be found elsewhere. In the case of a polar geometry and normal incidence, for example, the corresponding coefficients are tabulated in Ref. 21, whereas for a longitudinal geometry and oblique incidence, they are given in Ref. 22.

By exploiting in each layer the continuity of the tangential components of the total electric and magnetic field at the lower boundary z_p ($p=1, \ldots, N+1$) (see also Fig. 1), the layer-resolved reflectivity matrix $\mathcal{R}_p$, which relates all arbitrary electric field components to each other,

$$\mathcal{R}_{p} = (\mathcal{D}_{p-1}\mathcal{A}_{p}^{34} - \mathcal{B}_{p}^{34})^{-1}(\mathcal{B}_{p}^{12} - \mathcal{D}_{p-1}\mathcal{A}_{p}^{12}),$$

can be determined recursively by starting from the vanishing reflectivity matrix $\mathcal{R}_0=0$ of the substrate by means of the following 2×2 matrices:

$$\mathcal{A}_{p}^{k,k+1} = \begin{pmatrix} 1 & \tilde{\alpha}_{p}^{(k+1)} \\ \tilde{\alpha}_{p}^{(k)} & 1 \end{pmatrix}, \quad k = 1,3 \text{ and } p = 0, \ldots, N+1 \tag{15}$$

and

$$\mathcal{B}_{p}^{k,k+1} = \begin{pmatrix} n_y\tilde{\beta}_{p}^{(k)} - \tilde{n}_{pz}^{(k)}\tilde{\alpha}_{p}^{(k)} & n_y\tilde{\beta}_{p}^{(k+1)} - \tilde{n}_{pz}^{(k+1)} \\ \tilde{n}_{pz}^{(k)} - n_x\tilde{\beta}_{p}^{(k)} & \tilde{n}_{pz}^{(k+1)}\tilde{\alpha}_{p}^{(k+1)} - n_x\tilde{\beta}_{p}^{(k+1)} \end{pmatrix}, \quad k = 1,3 \text{ and } p = 0, \ldots, N+1. \tag{16}$$

Furthermore, also the propagation matrices,

$$\mathcal{C}_{p}^{k,k+1} = \begin{pmatrix} \exp[+iq_0\tilde{n}_{pz}^{(k)}d_p] & 0 \\ 0 & \exp[+iq_0\tilde{n}_{pz}^{(k+1)}d_p] \end{pmatrix}, \quad k = 1,3 \text{ and } p = 0, \ldots, N,$$

with $d_p = z_{p+1} - z_p > 0$ being the thickness of layer p, are needed to construct the auxiliary matrices:

$$\mathcal{D}_{p} = (\mathcal{B}_{p}^{12}\mathcal{C}_{p}^{12} + \mathcal{B}_{p}^{34}\mathcal{C}_{p}^{34}\mathcal{R}_{p})(\mathcal{A}_{p}^{12}\mathcal{C}_{p}^{12} + \mathcal{A}_{p}^{34}\mathcal{C}_{p}^{34}\mathcal{R}_{p})^{-1}, \quad p = 0, \ldots, N. \tag{17}$$

In vacuum, there are only two normal modes: an incident (i) and a reflected (r) one and, hence, the surface reflectivity matrix can be written as

$$\mathcal{R}_{\text{surf}} = \mathcal{R}_{N+1} = (\mathcal{D}_{N} - \mathcal{B}_{N+1}^{34})^{-1}(\mathcal{B}_{N+1}^{12} - \mathcal{D}_{N}) = \begin{pmatrix} \tilde{r}_{\text{xx}} & \tilde{r}_{\text{xy}} \\ \tilde{r}_{\text{yx}} & \tilde{r}_{\text{yy}} \end{pmatrix}, \tag{18}$$

where according to Eqs. (15) and (16),

$$\mathcal{B}_{N+1}^{12} = -\mathcal{B}_{N+1}^{34} = \frac{1}{\sqrt{1-(n_x^2+n_y^2)}} \begin{pmatrix} n_x n_y & 1-n_x^2 \\ -1+n_y^2 & -n_x n_y \end{pmatrix} \tag{19}$$

and

$$\mathcal{A}_{N+1}^{k,k+1} = \begin{pmatrix} 1 & 0 \\ 0 & 1 \end{pmatrix} = \boldsymbol{I}_{2\times 2}, \quad k = 1 \text{ and } 3. \tag{20}$$

In the case of transverse plane waves, the surface reflectivity matrix with respect to the local Cartesian coordinate system attached either to the incident or reflected wave is given by[23]

$$\mathsf{R}_{\text{surf}} = \mathcal{P}_{N+1}^{-1} \mathcal{R}_{\text{surf}} \mathcal{P}_{N+1} = \begin{pmatrix} \tilde{r}_{\text{pp}} & \tilde{r}_{\text{ps}} \\ \tilde{r}_{\text{sp}} & \tilde{r}_{\text{ss}} \end{pmatrix}, \tag{21}$$

where the transformation matrix is defined as

$$\mathcal{P}_{N+1} = \begin{pmatrix} \cos\theta\cos\varphi & -\sin\varphi \\ \cos\theta\sin\varphi & \cos\varphi \end{pmatrix}.$$

Because MOKE is fully described by the Kerr rotation θ_K and ellipticity angle ϵ_K, the amplitude and the absolute phase of the incident and the reflected light are of secondary interest. Therefore, the complex polarization variable,[24]

$$\tilde{\chi}_{[\text{p,s}]}^{(\text{r})} = \frac{\mathcal{E}_{N+1,\text{s}}^{(r)}}{\mathcal{E}_{N+1,\text{p}}^{(r)}} = \frac{\tilde{r}_{\text{sp}} + \tilde{r}_{\text{ss}}\tilde{\chi}_{[\text{p,s}]}^{(i)}}{\tilde{r}_{\text{pp}} + \tilde{r}_{\text{ps}}\tilde{\chi}_{[\text{p,s}]}^{(i)}}, \tag{22}$$

[see also Eq. (21)] completely characterizes the polarization state of the reflected wave, provided that the corresponding polarization variable on incidence,

$$\tilde{\chi}_{[\text{p,s}]}^{(\text{i})} = \frac{\mathcal{E}_{N+1,\text{s}}^{(\text{i})}}{\mathcal{E}_{N+1,\text{p}}^{(\text{i})}} = \frac{\tan\vartheta_{\text{i}} + i\tan\varepsilon_{\text{i}}}{1 - i\tan\vartheta_{\text{i}}\tan\varepsilon_{\text{i}}}, \tag{23}$$

is known in terms of the azimuth ϑ_{i} and ellipticity angle ε_{i} of the incident wave. Having determined by means of Eq. (22) the azimuth ϑ_{r} and ellipticity angle ε_{r} of the reflected light,

$$\tan 2\vartheta_{\text{r}} = \frac{2\,\text{Re}(\tilde{\chi}_{[\text{p,s}]}^{(\text{r})})}{1 - |\tilde{\chi}_{[\text{p,s}]}^{(\text{r})}|^2} \text{ and } \sin 2\varepsilon_{\text{r}} = \frac{2\,\text{Im}(\tilde{\chi}_{[\text{p,s}]}^{(\text{r})})}{1 + |\tilde{\chi}_{[\text{p,s}]}^{(\text{r})}|^2}, \tag{24}$$

the Kerr angles then directly result from[23]

$$\theta_K = \vartheta_{\text{r}} - \vartheta_{\text{i}} \text{ and } \epsilon_K = \varepsilon_{\text{r}} - \varepsilon_{\text{i}}. \tag{25}$$

III. COMPUTATIONAL DETAILS

From a computational point of view, the contributions $\tilde{\boldsymbol{\Sigma}}^{pq}(\omega)$ to the zero-wave-number current-current correlation function depend, besides the number of Matsubara poles for a given ω and T, also on both the number of complex energy points considered along the contour and on the number of $\vec{k}$ points used to compute the scattering path operator within the SKKR method.[25]

By applying the Konrod-Legendre rule (Appendix A) and the cumulative special-points method (Appendix B), it has been also shown[25] that the summed up contributions from the contour and Matsubara poles in the upper semiplane is a conserved quantity with an accuracy of $N_1\epsilon_{\vec{k}}$, where N_1 is the number of Matsubara poles in the upper semiplane and $\epsilon_{\vec{k}}$ is defined in Eq. (B3) of Appendix B. This independence of the optical conductivity tensor $\tilde{\boldsymbol{\sigma}}^{pq}(\omega)$ from the contour form in the upper semiplane is then exploited to significantly reduce the computational effort by considering $N_1 \gg N_2$, with N_2 being as small as possible, e.g., $N_2=2$.

The imaginary part of the Matsubara poles δ_T is the only quantity which directly depends on the electronic temperature T because of the Fermi-Dirac distribution function. In accordance with the applied constraint $\delta=2\delta_2$, when T varies, the lifetime broadening δ also changes. Thus, to preserve the broadening of bands involved in optical transitions, N_2 has to be taken as T dependent. However, to keep the difference N_1-N_2 large enough, e.g., 35 poles, N_1 has to change with T. Evaluations of the optical conductivity tensor for different T and $\delta=0.048$ Ryd (0.653 eV) kept fixed, however, have shown that, with the exception of some low photon energies, the T dependence of $\tilde{\boldsymbol{\sigma}}^{pq}(\omega)$ can be neglected.[15]

The present calculations of the magnetic properties of bcc Ni bulk and its (001) surface have been performed also by using the SKKR method; for a detailed review, see Ref. 4. Considering an overall lattice constant of $a=2.82$ Å, no attempt has been made to include eventual surface relaxations because, as recently shown by Khmelevskyi and Mohn,[26] a tetragonal distortion of the bcc Ni lattice not really changes its magnetic properties. The effective potentials were treated within the atomic sphere approximation using a local density approach (LDA) to DFT as parametrized in Ref. 27, and a cutoff $l_{\max}=2$ was used in all angular momentum expansions. For the SKKR self-consistent calculations, 16 energy points along a semicircular contour in the upper complex semiplane were used and 45 $\vec{k}_{\parallel}$ points in the irreducible wedge of the surface Brillouin zone (SBZ).

The lowest-order directional dependence of the energy in a ferromagnetic cubic system,

$$E(\vec{m}) = E_0 + K_1(m_x^2 m_y^2 + m_y^2 m_z^2 + m_x^2 m_z^2), \tag{26}$$

where $\vec{m}$ is a unit vector pointing along the magnetic moment and K_1 is the cubic magnetic anisotropy (MA) constant, implies that

$$K_1 = E(110) - E(100), \tag{27}$$

where $E(hkl)$ is the total energy for the case that the magnetization points uniformly along the (hkl) direction. This quantity has been evaluated in terms of the magnetic force theorem,[28]

$$K_1 = \sum_{p=1}^{N} K_1^p, \tag{28}$$

where K_1^p denotes the layer-resolved contribution to the MA constant, and N stands for the number of layers within the surfaced system. In order to obtain theoretical values K_1 within a relative accuracy of 5%, about 20 000 $\vec{k}_{\parallel}$ points in the SBZ were needed.

IV. RESULTS AND DISCUSSIONS

All results presented in this section were calculated for a photon energy $\omega=0.144$ Ryd $\simeq 1.9592$ eV, i.e., for a wavelength $\lambda=632.824\simeq 633$ nm typical for a He-Ne laser and with regards to a parametrization with $T=300$ K ($\delta_T=5.9693$ mRyd), $N_2=2$ ($\delta=0.048$ Ryd), and $N_1=N_2+35=37$.

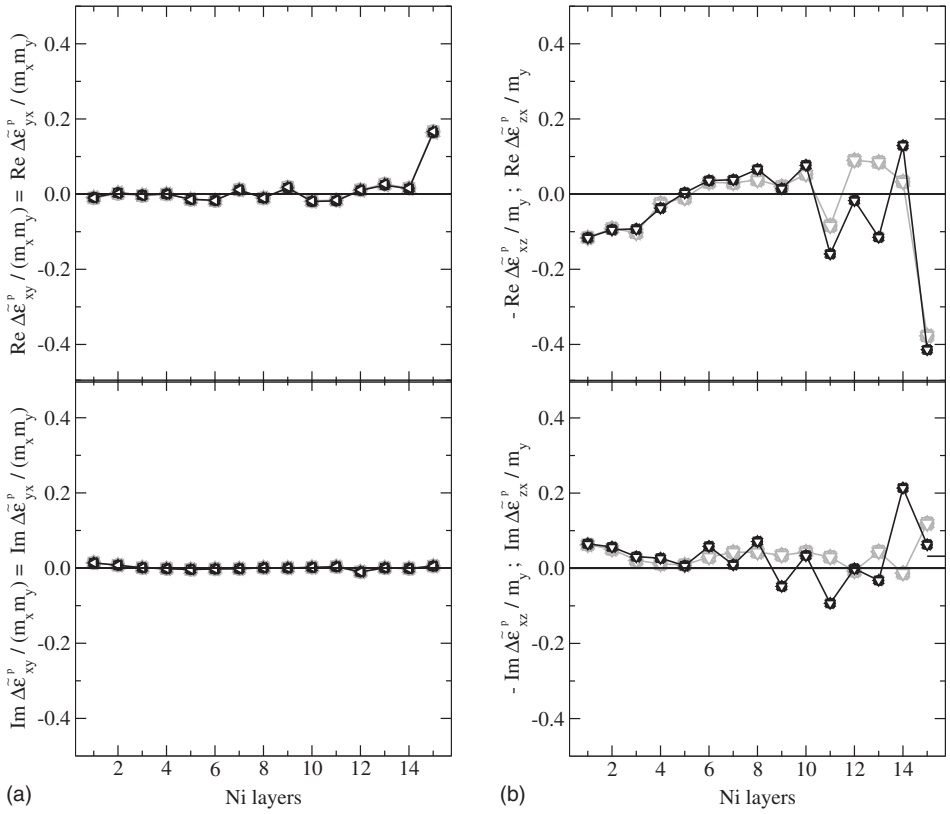

FIG. 2. Difference in the off-diagonal elements of the layer-resolved permittivities between bcc $Vac_3/Ni_{15}/Ni(100)$ and bcc $Ni(100)/Ni_{24}/Ni(100)$ for a photon wavelength $\lambda \simeq 633$ nm. Circles, squares, diamonds, and triangles (up, left, and down) refer to $\varphi_{\vec{M}} = 15°$, 30°, 45°, 60°, 75°, and 90° [see Eqs. (29) and (30)]. Black symbols correspond to the first label on the ordinate, gray symbols to the second one. The layer numbering starts with the first layer on top of the semi-infinite bulk substrate.

Assuming the semi-infinite bcc Ni bulk (lattice parameter of 2.82 Å) as an electron reservoir, the self-consistently determined Fermi level of bcc Ni bulk has been used in all calculations.

A. Layer-resolved permittivities

Having determined all inter- and intralayer contributions to the complex optical conductivity, Eqs. (8) and (9) directly provide the layer-resolved permittivities. For bcc $Vac_{N_{vac}}/Ni_{N_{lay}}/Ni(100)$ layered system, they are of the form

$$\tilde{\boldsymbol{\varepsilon}}^p = \begin{pmatrix} \tilde{\varepsilon}^p_{xx} & \tilde{\varepsilon}^p_{xy} m_x m_y & -\tilde{\varepsilon}^p_{xz} m_y \\ \tilde{\varepsilon}^p_{xy} m_x m_y & \tilde{\varepsilon}^p_{xx} & \tilde{\varepsilon}^p_{xz} m_x \\ \tilde{\varepsilon}^p_{zx} m_y & -\tilde{\varepsilon}^p_{zx} m_x & \tilde{\varepsilon}^p_{zz} \end{pmatrix}, \quad \forall\, p = 1, \ldots, N = N_{\text{lay}} + N_{\text{vac}}. \tag{29}$$

The dimensionless quantities $\tilde{\varepsilon}^p_{\mu\nu} \in \mathbb{C}$ (μ, $\nu = x$, y, z and $\forall p = 0, 1, \ldots, N_{\text{lay}} + N_{\text{vac}}$) are independent of the polar angle $\varphi_{\vec{M}}$ between the x axis and the uniform in-plane magnetizations $\vec{M}_p$. In Eq. (29), $m_x = \cos\varphi_{\vec{M}}$ and $m_y = \sin\varphi_{\vec{M}}$ denote the normalized Cartesian components of $\vec{M}_p$ for $\forall p = 0, 1, \ldots, N$, with $N = N_{\text{lay}} + N_{\text{vac}}$.

A slightly different tensor form than that in Eq. (29) applies for the permittivity of the substrate viewed as a bcc $Ni(100)/Ni_{N_0}/Ni(100)$ layered system,

$$\tilde{\boldsymbol{\varepsilon}}^0 = \begin{pmatrix} \tilde{\epsilon}^0_{xx} & \tilde{\epsilon}^0_{xy} m_x m_y & -\tilde{\epsilon}^0_{xz} m_y \\ \tilde{\epsilon}^0_{xy} m_x m_y & \tilde{\epsilon}^0_{xx} & \tilde{\epsilon}^0_{xz} m_x \\ \tilde{\epsilon}^0_{xz} m_y & -\tilde{\epsilon}^0_{xz} m_x & \tilde{\epsilon}^0_{zz} \end{pmatrix}. \tag{30}$$

Here and in the following, N_0 denotes the total number of Ni layers in between two semi-infinite bcc Ni(100) systems.

Note that the higher symmetry of $\tilde{\boldsymbol{\varepsilon}}^0$ in comparison with $\tilde{\boldsymbol{\varepsilon}}^{p\neq 0}$ is a consequence of the symmetrization for the N_0 layer-resolved permittivities, which, as shown elsewhere,[29] is absolutely necessary to determine uniquely the permittivity of the substrate.

Therefore, independent of the unique direction of the in-plane layer-resolved magnetizations, the difference between the layer-resolved permittivities and that of the substrate,

$$\Delta\tilde{\boldsymbol{\varepsilon}}^p = \tilde{\boldsymbol{\varepsilon}}^p - \tilde{\boldsymbol{\varepsilon}}^0, \quad \forall\, p = 1, \ldots, N_{\text{lay}} + N_{\text{vac}}, \tag{31}$$

can be viewed as a measure of the surface sensitivity in bcc $Vac_{N_{vac}}/Ni_{N_{lay}}/Ni(100)$. Indeed, Figs. 2 and 3 fully confirm that the larger $\Delta\tilde{\boldsymbol{\varepsilon}}^p$, the closer is the layer p to the surface. Furthermore, these figures show that, with the exception of $\Delta\tilde{\varepsilon}^p_{xy} = \Delta\tilde{\varepsilon}^p_{yx}$, which are negligible for $\forall p = 1, \ldots, N-1$, the

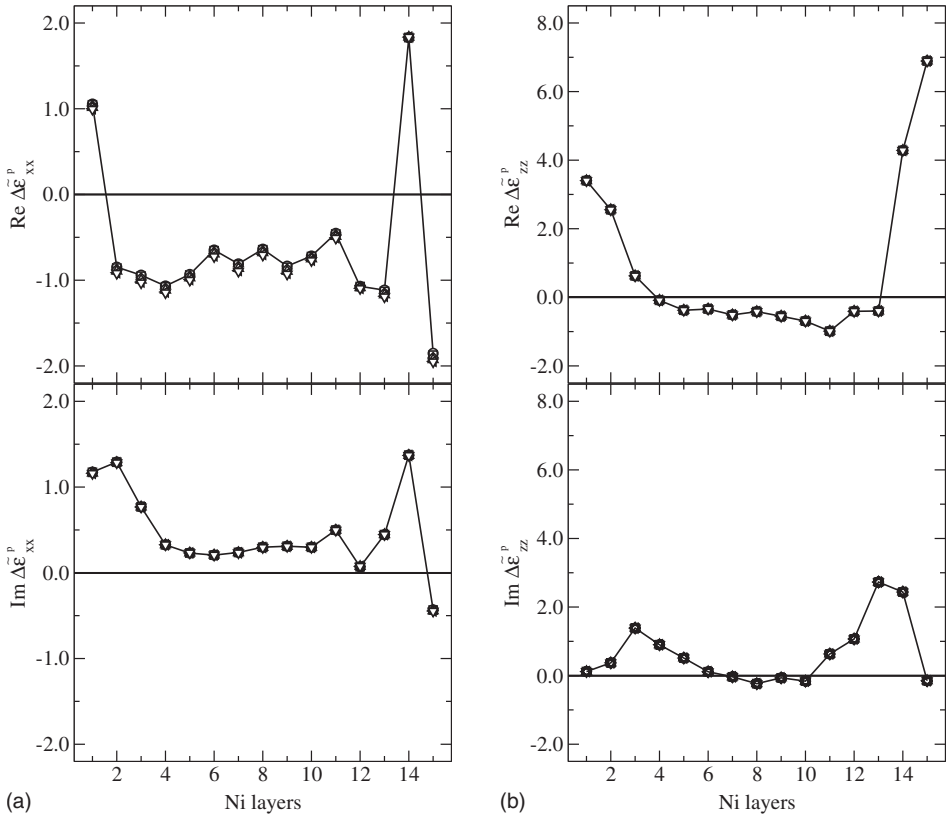

FIG. 3. As in Fig. 2, but for the diagonal elements. Not shown here is $\Delta\tilde{\boldsymbol{\varepsilon}}^p_{yy}=\Delta\tilde{\boldsymbol{\varepsilon}}^p_{xx}$.

diagonal elements of the layer-resolved permittivities are more affected by the surface than the off-diagonal ones. Not shown in Fig. 2 are the off-diagonal tensor elements $\Delta\tilde{\boldsymbol{\varepsilon}}^p_{yz} \equiv \Delta\tilde{\boldsymbol{\varepsilon}}^p_{yz}/m_x$ and $\Delta\tilde{\boldsymbol{\varepsilon}}^p_{zy} \equiv \Delta\tilde{\boldsymbol{\varepsilon}}^p_{zy}/m_x$, because they are identical to $-\Delta\tilde{\boldsymbol{\varepsilon}}^p_{xz} \equiv -\Delta\tilde{\boldsymbol{\varepsilon}}^p_{xz}/m_y$ and $-\Delta\tilde{\boldsymbol{\varepsilon}}^p_{zx} \equiv -\Delta\tilde{\boldsymbol{\varepsilon}}^p_{zx}/m_y$, respectively. The $\Delta\tilde{\boldsymbol{\varepsilon}}^p$ show a two-layer periodicity typical for the *ABAB*… stacking of a bcc (100) surface. The amplitude of these oscillations, however, is more attenuated near the substrate than in the vicinity of the surface.

B. Kerr angles for oblique incidence

In the following, *ab initio* Kerr angles are presented for a linearly polarized light ($\lambda \simeq 633$ nm, i.e., $\omega=0.144$ Ryd $\simeq 1.9592$ eV) at oblique incidence within the $0yz$ plane, namely, for $0 \leqslant \theta \leqslant 90°$ and $\varphi=90°$ in Eq. (11) as obtained by applying the 2×2 matrix technique.

The permittivity $\tilde{\boldsymbol{\varepsilon}}^0$ of the substrate was obtained using a perfect two-dimensional periodic infinite $\mathrm{Ni(100)/Ni_{24}/Ni(100)}$ layered system; the layer-resolved permittivities $\tilde{\boldsymbol{\varepsilon}}^p$ of the surface system correspond to semi-infinite bcc $\mathrm{Vac_3/Ni_{15}/Ni(100)}$. All permittivity calculations have been repeated for all directions considered here, namely, for polar angles $\varphi_{\vec{M}}$ specifying the direction of the in-plane layer-resolved magnetizations with respect to the x axis, and were varied in the first quadrant [0, 90°] by a step of 15°.

The $\varphi_{\vec{M}}$ dependence of the so-calculated Kerr angles for a p-polarized incident light and different angles of incidence θ is shown in Fig. 4. A similar linear behavior of m_l-scaled Kerr angles as a function of m_t,

$$m_\mathrm{l} = \sin\varphi_{\vec{M}}, \qquad m_\mathrm{t} = \cos\varphi_{\vec{M}}, \tag{32}$$

has also been obtained for an s-polarized incident light, independent of its handedness, with Kerr angles being identical for left- and right-handed s waves, respectively. This latter feature is easily understood when using the well-known approximation[23] $\theta_{K,s} - i\varepsilon_{K,s} \simeq \tilde{r}_\mathrm{ps}/\tilde{r}_\mathrm{ss}$ to determine the Kerr angles $\theta_{K,s}$ and $\varepsilon_{K,s}$, because in the case of bcc Ni/Ni(100), the incident azimuth dependence of the complex reflectivity coefficients $\tilde{r}_\mathrm{ps}$ and $\tilde{r}_\mathrm{ss}$ is really negligible.

Comparing the Kerr data for different linearly polarized incident light, one can observe that the m_l dependence of the Kerr angles is, by far, more pronounced for an s-polarized incident light than for a p one, and the θ dependence of Kerr angles is also incident polarization dependent. For example, as long as for any unique direction of all layer-resolved magnetizations the Kerr rotation angle achieves a maximum at $\theta=55°$ when a p-polarized light is in use, the largest $\theta_{K,s}$ occurs for an angle of incidence of 70°.

In spite of all these dependencies, the calculated Kerr angles for any $\varphi_{\vec{M}}$ are well reproduced by the appropriate expressions:[2]

$$\theta_K = \theta^\mathrm{l}_K m_\mathrm{l} + \theta^\mathrm{q}_K m_\mathrm{l} m_\mathrm{t},$$

$$\varepsilon_K = \varepsilon^\mathrm{l}_K m_\mathrm{l} + \varepsilon^\mathrm{q}_K m_\mathrm{l} m_\mathrm{t}, \tag{33}$$

containing both linear θ^l_K, ε^l_K and quadratic θ^q_K, ε^q_K Fresnel coefficients,[30] which, however, are only functions of the incidence angle θ. In Eq. (33), the linear Fresnel coefficients describe the contribution to the amplitude of the linear

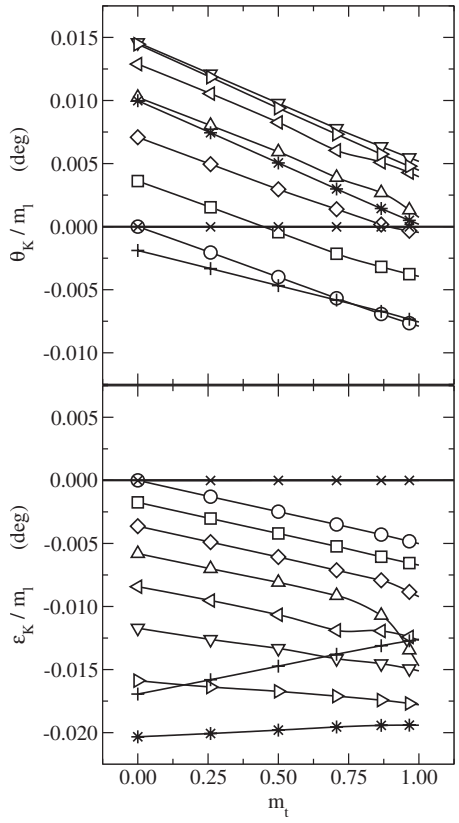

FIG. 4. Kerr angles for bcc Ni/Ni(100) scaled by the normalized longitudinal magnetization component $m_l = \sin \varphi_{\vec{M}}$ for an oblique incidence of a p-polarized light in the $0yz$ plane ($\lambda \simeq 633$ nm) and bcc Ni/Ni(100) as a function of the normalized transverse component $m_t = \cos \varphi_{\vec{M}}$. Circles, squares, diamonds, and triangles (up, left, down, and right) refer to Kerr angles calculated for an angle of incidence $\theta = 0, 10, \ldots, 60°$ (open symbols); stars, pluses, and crosses correspond to $\theta = 70°$, 80°, and 90°.

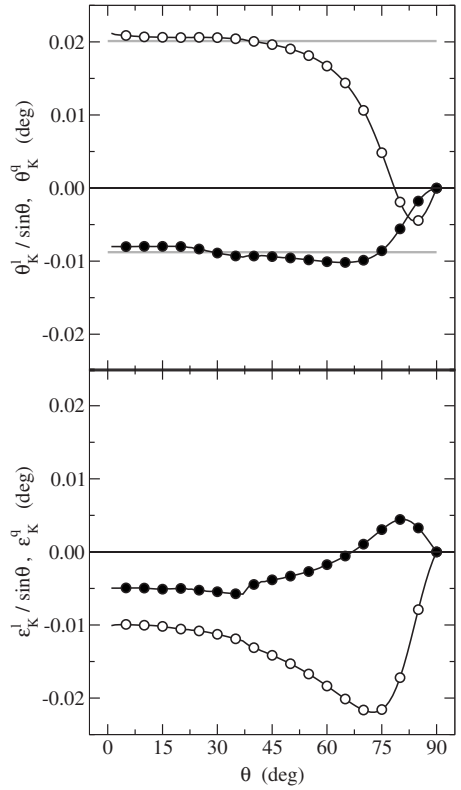

FIG. 5. Fresnel coefficients for p-polarized light incident within the $0yz$ plane ($\lambda \simeq 633$ nm) in bcc Ni/Ni(100) as a function of the angle of incidence θ [see Eqs. (33)–(35)]. sin θ scaled linear and plain quadratic Fresnel coefficients are shown by open and full circles, respectively.

MOKE, whereas the quadratic Fresnel coefficients determine the quadratic MOKE part in the Kerr angles.

Having calculated the Kerr angles $\eta_K(\varphi_{\vec{M}})$, with $\eta_K \equiv \theta_K$ or ε_K, for n values of the longitude $\varphi_{\vec{M}}$, i.e., by assuming all $\eta_K(\varphi_{\vec{M}}^{(j)}) \in \mathbb{R}$ for $j = 1, \ldots, n$ known, within a least-squares fitting method,[31] the Fresnel coefficients entering Eq. (33) can be viewed as adjustable parameters which minimize the merit (chi-square) function

$$\chi^2 = \sum_{j=1}^{n} \{\eta_K(m_l^{(j)}, m_t^{(j)}) - [\eta_K^l m_l^{(j)} + \eta_K^q m_l^{(j)} m_t^{(j)}]\}^2 \quad (34)$$

and, hence, can directly be obtained by solving a set of linear equations corresponding to the extremum conditions:

$$\frac{\partial \chi^2}{\partial \eta_K^l} = -2 \sum_{j=1}^{n} \{\eta_K(m_l^{(j)}, m_t^{(j)}) - [\eta_K^l m_l^{(j)} + \eta_K^q m_l^{(j)} m_t^{(j)}]\} m_l^{(j)} = 0,$$

$$\frac{\partial \chi^2}{\partial \eta_K^q} = -2 \sum_{j=1}^{n} \{\eta_K(m_l^{(j)}, m_t^{(j)}) - [\eta_K^l m_l^{(j)} + \eta_K^q m_l^{(j)} m_t^{(j)}]\} m_l^{(j)} m_t^{(j)} = 0. \quad (35)$$

Note that the deviations made in calculating $\eta_K(m_l^{(j)}, m_t^{(j)})$ have not been taken into account and, therefore, in Eq. (34), all standard deviations σ_j, $\forall j = 0, 1, \ldots, n$, have been set equal to 1.

The main advantage of the least-squares fitting method is that per definition any deviation of used data from their general trend is corrected. By testing this feature for a relatively small bcc $Vac_3/Ni_6/Ni(100)$ layered system, it is, therefore, not at all surprising that the Kerr angles determined by using Eq. (33) with Fresnel coefficients obtained for a finite mesh of $\Delta\varphi_{\vec{M}} = 15°$ or $\Delta\varphi_{\vec{M}} = 5°$, respectively, turned out to be identical. This, in turn, shows that an increment of $\Delta\varphi_{\vec{M}} = 15°$ is sufficient to determine highly accurate Fresnel coefficients even for large systems.

The θ dependence of the Fresnel coefficients in Fig. 5 has been calculated via the least-squares fitting method using an increment of $\Delta\theta = 1°$. This fine mesh guaranteed to accurately determine values of θ at which particularities of Fresnel coefficients occur. For example, besides $\theta = 0$ and 90° for which quite clearly the linear Fresnel coefficients vanish, θ_K^l is also zero when $\theta = 78°$. Furthermore, extrema of θ_K^l are

achieved for $\theta=55°$ (maximum) and 84° (minimum), but the smallest value of θ_K^{q} corresponds to $\theta=54°$.

The fact that the linear Fresnel coefficients show a simple $\sin\theta$ dependence with respect to the angle of incidence θ is well known in the literature,[32] but is only partially confirmed by our *ab initio* calculations, namely,

$$\theta_K^{\mathrm{l}} = \Theta_K^{\mathrm{l}} \sin\theta, \quad \theta \leqslant 55°,$$

$$\epsilon_K^{\mathrm{l}} \sim \sin\theta, \quad \theta \leqslant 35°, \tag{36}$$

where Θ_K^{l} is independent of θ. By assuming that

$$|\Theta_K^{\mathrm{l}}| \sim |\vec{M}|, \qquad |\theta_K^{\mathrm{q}}| \sim |\vec{M}|^2, \tag{37}$$

with $\vec{M}$ being the averaged magnetization of the layered system

$$\vec{M} = \frac{1}{N}\sum_{p=1}^{N} \vec{M}_p, \tag{38}$$

where the layer-resolved magnetizations $\vec{M}_p$ differ only in magnitude, then in accordance with Eqs. (36) and (37),

$$\left|\frac{\theta_K^{\mathrm{q}}}{\Theta_K^{\mathrm{l}}}\right| \sim |\vec{M}| \tag{39}$$

at least for $\forall\,\theta \leqslant 55°$. The calculated averaged total magnetic moment,

$$\vec{\mu} = \frac{1}{N}\sum_{p=1}^{N} \vec{\mu}_p, \tag{40}$$

with the layer-resolved total magnetic moment $\vec{\mu}_p$ containing both in-plane spin and orbital moments from a layer p, amounts for bcc $\mathrm{Vac}_3/\mathrm{Ni}_{15}/\mathrm{Ni}(100)$ to $|\vec{\mu}|=0.6562\ \mu_B$/atom (see Fig. 9). In view of Eqs. (38)–(40), therefore

$$1.5 \simeq \frac{\bar{\mu}}{\left|\dfrac{\theta_K^{\mathrm{q}}}{\Theta_K^{\mathrm{l}}}\right|_{\mathrm{av}}} \sim \Omega, \tag{41}$$

where Ω is a characteristic (reference) volume in each layer p such as, for example, the volume of the Wigner-Seitz (WS) sphere $4\pi R_{\mathrm{WS}}^3/3$, with $R_{\mathrm{WS}}=2.624a_0$ in the case of bcc Ni (Bohr radius $a_0=0.5292$ Å).

Having obtained highly accurate Fresnel coefficients, Eq. (33) can directly be used to determine Kerr angles for an arbitrary direction in any quadrant of the $0xy$ plane. The Kerr rotation angle, e.g., is shown in Fig. 6. As can be seen from this figure, for angles of incidence $\theta \in [0,23°]\cup[70°,82°]$, the Kerr rotation angle as a function of $\varphi_{\vec{M}}$ has four extrema, whereas for $\theta \in (23°,70°)\cup(82°,90°]$, there are only two. According to the appropriate formulas for the Kerr angles given by Eq. (33), extrema of $\eta_K(\varphi_{\vec{M}})$ occur, e.g., either when $\eta_K=\theta_K$ or $\eta_K=\varepsilon_K$, if the first derivative of $\eta_K(\varphi_{\vec{M}})$ with respect to the polar angle $\varphi_{\vec{M}}$ vanishes, i.e.,

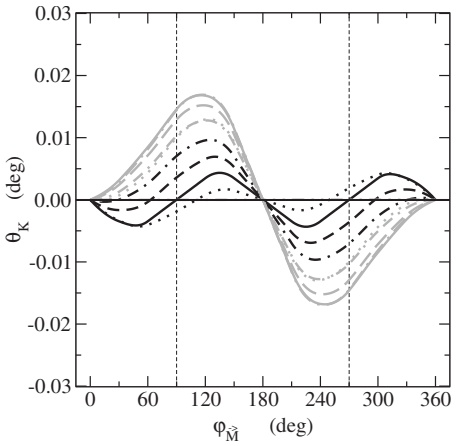

FIG. 6. Kerr rotation angle θ_K for oblique incidence and p-polarized light within the $0yz$ plane ($\lambda \simeq 633$ nm) in bcc Ni/Ni(100) as a function of the polar angle $\varphi_{\vec{M}} \in [0,360°]$ between the x axis and the uniform in-plane magnetization. Black full, dashed, dash-dotted, and dotted lines refer to Kerr rotation angles showing four extrema, i.e., for an angle of incidence $\theta=0$, 10°, 20°, and 80°, whereas gray dash-dotted, dashed, continuous, dot–long dashed, dotted, and double dot–dashed lines correspond to $\theta=30°$, 40°, 50°, 60°, 70°, and 90°, for which the Kerr rotation angle has only two extrema.

$$\frac{\partial\eta_K(\varphi_{\vec{M}})}{\partial\varphi_{\vec{M}}} = 2\eta_K^{\mathrm{q}} m_{\mathrm{t}}^2 + \eta_K^{\mathrm{l}} m_{\mathrm{t}} - \eta_K^{\mathrm{q}} = 0. \tag{42}$$

According to Eq. (42), an extremum of the Kerr angles is achieved when the normalized transverse component of all in-plane layer-resolved magnetizations is given by

$$m_{\mathrm{t}}^{(\pm)} = -\frac{\eta_K^{\mathrm{l}}}{4\eta_K^{\mathrm{q}}} \pm \sqrt{\frac{1}{2}+\left(\frac{\eta_K^{\mathrm{l}}}{4\eta_K^{\mathrm{q}}}\right)^2} \quad (\eta_K^j=\theta_K^j,\varepsilon_K^j;\ j=1 \text{ and q}), \tag{43}$$

which is the case for one of the four polar angles

$$\varphi_{\vec{M}}^s = \pm\arccos[m_{\mathrm{t}}^{(\pm)}] + 2k\pi, \quad k\in\mathbb{Z} \quad (s=1,2,3, \text{ and } 4), \tag{44}$$

provided that $|m_{\mathrm{t}}^{(\pm)}| \leqslant 1$. In terms of Eq. (44), one would expect, therefore, that always four extrema of θ_K occur. However, this is not always the case, although in Eq. (43) the discriminant is a strictly positive quantity,

$$\frac{1}{2}+\left(\frac{\eta_K^{\mathrm{l}}}{4\eta_K^{\mathrm{q}}}\right)^2 > 0,$$

and the cosine an even function. The reason for this is the criterion $|m_{\mathrm{t}}^{(\pm)}| \leqslant 1$ which additionally limits the number of extrema to be observed for the Kerr angles (see Fig. 7). By recalling Eq. (39), one also notes that Eqs. (43) and (44) yield the extrema of the Kerr angles when parametrized by a quarter of the inverse magnitude of the average magnetization.

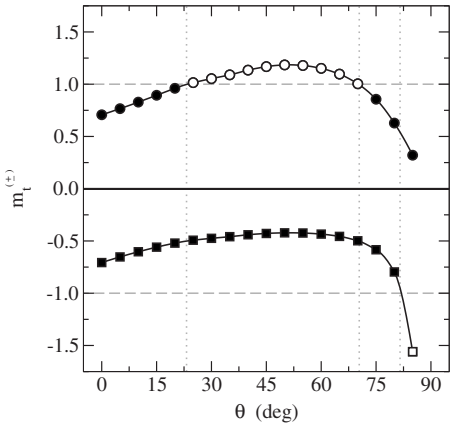

FIG. 7. Normalized transverse component of the uniform in-plane magnetization that corresponds to the extrema of the Kerr rotation angle for oblique incidence and *p*-polarized light within the $0yz$ plane ($\lambda \simeq 633$ nm) in bcc Ni/Ni(100) as a function of the incidence angle θ. Circles and squares denote values of $m_t^{(\pm)}$ obtained by using the θ dependence of Fresnel coefficients shown in Fig. 5. Open symbols mark $m_t^{(\pm)}$ values out of range $[-1,1]$. Gray dotted lines denote intervals of θ in between which the Kerr rotation angle has either four or two extrema.

Further features of the Kerr rotation angle in Fig. 6 can be deduced by exploiting in Eq. (33) the symmetry properties of the normalized magnetization components m_l and m_t. By taking $\varphi_{\vec{M}}+180°$ in Eq. (33), one gets

$$\eta_K(\varphi_{\vec{M}} + 180°) = \eta_K(\varphi_{\vec{M}}) - 2\eta_K^l m_l, \tag{45}$$

which, in turn, immediately yields a linear Fresnel coefficient η_K^l, provided that the layer-resolved in-plane magnetizations are not in a direction for which m_l vanishes. On the other hand, once η_K^l is known, the quadratic Fresnel coefficient η_K^q can directly be evaluated by using

$$\eta_K^q = \frac{\eta_K(\varphi_{\vec{M}}) - \eta_K^l m_l}{m_l m_t}, \tag{46}$$

if in addition to $m_l \neq 0$, also $m_t \neq 0$. From a formal point of view, Eq. (45) shows that it is enough to calculate $\eta_K(\varphi_{\vec{M}})$ $\forall \varphi_{\vec{M}} \in [0,180°]$ in order to cover the complete interval $[0, 360°]$. Similarly, from Eq. (33) also results

$$\eta_K(\varphi_{\vec{M}} + 90°) = \eta_K^l(m_l + m_t) - \eta_K(\varphi_{\vec{M}}),$$

which means that one needs only $\eta_K(\varphi_{\vec{M}})$ $\forall \varphi_{\vec{M}} \in [0,90°]$ to get Kerr angles also $\forall \varphi_{\vec{M}} \in [90°,180°]$. The quadratic Fresnel coefficient, on the other hand, follows directly from Eq. (46).

Altogether this not only fully confirms our choice of limiting the polar angle to $\varphi_{\vec{M}} \in [0,90°]$ when calculating the Kerr angles, but also explains why it is possible to successfully determine Kerr angles for any other uniform direction of layer-resolved in-plane magnetizations.

C. Two-media approach

All macroscopic models, which from an optical point of view approximate reasonably well any semi-infinite layered system, involve fewer number of interfaces to account for when describing multiple reflections and optical interferences than the initial one. Common in all these optical models, however, is the presence of a semi-infinite substrate of known permittivity $\tilde{\boldsymbol{\varepsilon}}^0$. Because there are no interfaces in the substrate of thickness $d_0=+\infty$, its reflectivity matrix $\mathcal{R}_0=0$ and, hence, according to Eq. (17)

$$\mathcal{D}_0 = \mathcal{B}_0^{12}(\mathcal{A}_0^{12})^{-1}, \tag{47}$$

where both matrices $\mathcal{A}_0^{12}$ and $\mathcal{B}_0^{12}$ directly follow from Eqs. (15) and (16) using coefficients $\tilde{\alpha}_0^{(k)}$ and $\tilde{\beta}_0^{(k)}$ ($k=1$ and 2) as determined by solving Eqs. (10) and (12) in terms of $\tilde{\boldsymbol{\varepsilon}}^0$, θ, and φ.

In the case of a homogeneous layered system consisting of identical layers, it has been shown elsewhere[29] that, at least for polar geometry and normal incidence, our 2×2 matrix technique yields the well-known Fresnel formula for the complex reflectivity coefficients. Formally, one deals with $N=0$ layers such that the surface reflectivity matrix within the two-media approach can be written as

$$\mathcal{R}_{\text{surf}}^{[2]} = \mathcal{R}_1 = (\mathcal{D}_0 - \mathcal{B}_1^{34})^{-1}(\mathcal{B}_1^{12} - \mathcal{D}_0), \tag{48}$$

[see Eq. (18)] because $\mathcal{A}_1^{34}=\mathcal{A}_1^{12}=\boldsymbol{I}_{2\times2}$, with $\boldsymbol{I}_{2\times2}$ being the 2×2 identity matrix [see Eq. (20)]. Quite obviously, in Eq. (48) the matrices $\mathcal{B}_1^{12}$ and $\mathcal{B}_1^{34}$ refer to those in Eq. (19), and $\mathcal{D}_0$ is given by Eq. (47).

The difference between the Kerr angles η_K ($\eta_K=\theta_K$ or ε_K) obtained by applying the 2×2 matrix technique and the corresponding angles $\eta_K^{[2]}$ resulting from the two-media approach unambiguously reveals the contribution of the surface to the MOKE. As can be seen from Fig. 8, these contributions are not only extremely significant, but represent the major part of the magnitude of the Kerr angles. Furthermore, a detailed analysis has shown that about 75% of the linear Fresnel coefficients are due to the presence of the surface. Finally, it should be noted that only for a normal incidence, the Kerr angles calculated via the 2×2 matrix technique and using the two-media approach, respectively, are identical.

D. Magnetic moments and magnetic anisotropy

In Ref. 1, the magnetic properties of a 3.5 nm bcc Ni/GaAs(001) sample has been investigated. In terms of super conducting quantum interference device measurements, the magnetic moment of Ni was found to be $0.52\pm0.08\mu_B$, while from ROTMOKE measurements, a magnetic cubic anisotropy of $K_1=4.0\times10^5$ erg cm^{-3} has been deduced, which for the experimental lattice constant $a=2.82$ Å of bcc Ni corresponds to an anisotropy constant $K_1=2.8$ μeV/atom.

Our calculations lead to a spin magnetic moment of $0.59\mu_B$ for bcc Ni bulk, which although is slightly larger than the experimental one is in good agreement with the scalar-relativistic value of $0.54\mu_B$ reported in Refs. 26 and 33. According to our relativistic calculations, the orbital magnetic moment is $0.054\mu_B$. Our MA calculations [see Eqs. (26) and (27)] correctly predict the easy axis to be the (100) one; however, the calculated value for $K_1=10^{-2}$ μeV/atom is by 2 orders of magnitude smaller than the experimentally deduced value.

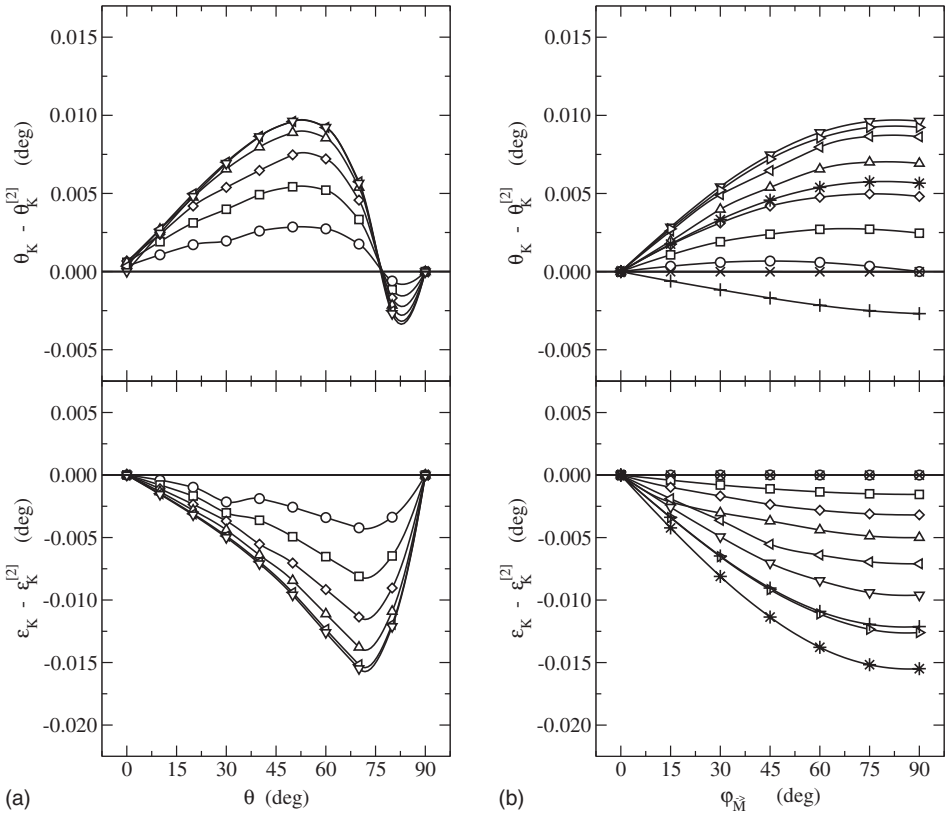

FIG. 8. Differences in the Kerr angles for oblique incidence of *p*-polarized light in $0yz$ plane ($\lambda \simeq 633$ nm) and bcc Ni/Ni(100) when using the 2×2 matrix technique and the two-media approach as a function of the incidence angle θ (left) or the polar angle $\varphi_{\vec{M}}$ (right). In the left panel, circles, squares, diamonds, and triangles (up, left and down) refer to Kerr angles obtained for a polar angle $\varphi_{\vec{M}}=15°$, 30°, 45°, 60°, 75°, and 90° (open symbols); in the right panel, circles, squares, diamonds, and triangles (up, left, down, and right) represent Kerr angles obtained for an angle of incidence $\theta=0,10,\ldots,60°$ (open symbols); stars, pluses, and crosses stand for $\theta=70°$, 80°, and 90°.

It is well known that by including a heuristic orbital polarization (OP) contribution[34] into the LDA, a substantial improvement in both the calculated orbital moments and MA energies, respectively, can be achieved in the case of ferromagnetic bulk materials.[35] By adapting the OP potential scheme of Ref. 36 to our relativistic SKKR method, the so-obtained MA constant $K_1=0.84$ μeV/atom is only about one-third of the experimental value given in Ref. 1. Note also that by including the OP term, a moderately enhanced orbital magnetic moment of $0.079\mu_B$ has been obtained in comparison to the LDA result.

As already mentioned, the measurements in Ref. 1 are for a probe thickness of 3.5 nm, i.e., for an about 25 ML thick Ni film. Therefore, the MA constant deduced from the torque measurements via ROTMOKE corresponds to an average value over the entire film, which consists of the surface/interface and the interior (bulklike) regions. In order to relate this average to the bulk value, also calculations for the (001) surfaced bcc Ni have been performed, revealing an enhancement of $0.76\mu_B$ and $0.23\mu_B$, respectively, in the Ni surface layer with respect to the bulk values of the spin and orbital magnetic moments (see Fig. 9). The moments then rapidly decreased with the distance from the surface such that all layers below the seventh one are, in fact, bulklike.

As can be seen from Fig. 10, the layer-resolved contributions to the MA constant with respect to the number of layer strongly oscillate and converge very slowly to the calculated bulk value. In particular, the in-plane MA constant at the surface layer is nearly 20 μeV/atom, i.e., is more than 20 times larger than in the bulk. Quite clearly, then for even a very thick bcc Ni film, the layer averaged MA,

$$\bar{K}_1^p = \frac{1}{N+1-p}\sum_{q=p}^{N} K_1^q, \tag{49}$$

[recall Eq. (28)] will always be much larger than the bulk MA constant. It is worthwhile to note that the averaged theoretical MA constant approaches the experimental bulk value only after 12–13 monolayers of Ni. Considering that in the experiment a larger system of about 25 monolayers of bcc Ni on GaAs(001) was used, the MA constant as experimentally determined by applying the ROTMOKE seems to be strongly overestimated.

V. SUMMARY

By using the Luttinger formula and the spin-polarized relativistic screened Korringa-Kohn-Rostoker method, the inter- and intralayer contributions $\tilde{\boldsymbol{\sigma}}^{pq}(\omega)$ to the complex optical conductivity have been computed for a photon wavelength $\lambda=633$ nm and in bcc $\mathrm{Vac}_{N_{\mathrm{vac}}}/\mathrm{Ni}_{N_{\mathrm{lay}}}/\mathrm{Ni}(100)$ surface and $\mathrm{Ni}(100)/\mathrm{Ni}_{N_{\mathrm{lay}}}/\mathrm{Ni}(100)$ for different in-plane magnetiza-

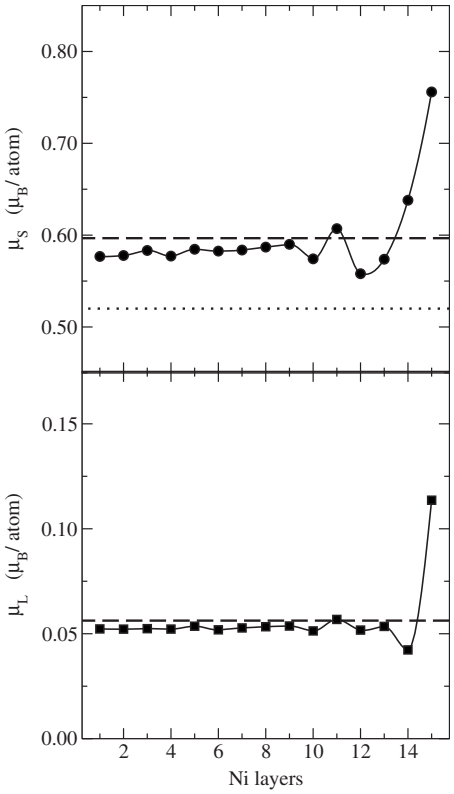

FIG. 9. Layer-resolved spin (circles) and orbital (squares) magnetic moments in bcc $Vac_3/Ni_{15}/Ni(100)$. Dashed and dotted lines mark the corresponding averaged *ab initio* moments and the experimental spin moment (Ref. 1), respectively. Layer 15 corresponds to the surface Ni layer.

tion orientations. In comparing the layer-resolved permittivities with that of the semi-infinite bulk substrate, it was shown that, with the exception of the *xy* components, all other permittivity tensor elements are dominated by contributions arising from the surface.

Ab initio Kerr angles obtained via the 2×2 matrix technique for an arbitrary linearly polarized light at oblique incidence within the $0yz$ plane proved that the appropriate formulas for Kerr angles widely used in the literature are valid for a relatively large range of incidence angles and are independent of the polarization of the incident light. The calculated Fresnel coefficients showed that besides the magnitude of the average magnetization, they only depend on the angle of incidence θ. Within the range of validity of the appropriate formulas, the θ dependence of the linear Fresnel coefficients was found to scale as $\sin\theta$, confirming the experimental expectation, whereas the quadratic Fresnel coefficients are almost independent of θ. With these highly accurate Fresnel coefficients, the appropriate formulas can be applied to determine Kerr angles for any arbitrary direction of a uniform in-plane magnetization. A comparison of the calculated Kerr angles via the 2×2 matrix technique with those determined by using the two-media approach has evidenced that the latter only applies for a normal incidence, whereas for arbitrary oblique incidences, about 75% of the magnitude of Kerr rotation angles arises from surface contributions.

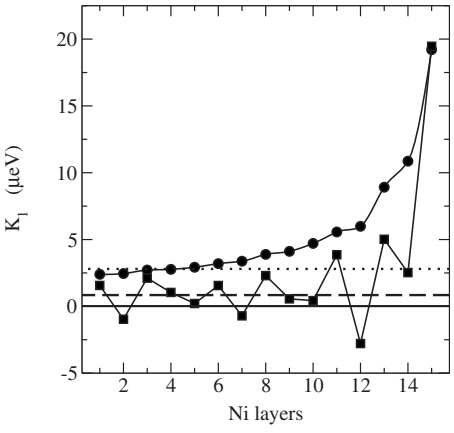

FIG. 10. Layer-resolved in-plane magnetic anisotropy constants (circles) and their averaged value (squares) in bcc $Vac_3/Ni_{15}/Ni(100)$. Dashed and dotted lines refer to the *ab initio* and experimental (Ref. 1) cubic anisotropy constants, respectively. Layer 15 corresponds to the surface Ni layer.

Furthermore, magnetic anisotropy calculations led to oscillating layer-resolved cubic magnetic anisotropy constants dominated by contributions from layers situated near the surface on the vacuum side. The average magnetic anisotropy constant, however, is in good agreement with that derived from ROTMOKE measurements. However, not even this quantity can be unambiguously identified with that obtained for bcc Ni bulk.

ACKNOWLEDGMENTS

Financial support from the Austrian Science Foundation (FWF, Project No. WK W004), from the Vienna University of Technology, and from the Hungarian National Science Foundation (Nos. OTKA T46267 and K68312) is gratefully acknowledged.

APPENDIX A: KONROD QUADRATURE

Although the Gauss-Legendre integration rule can be immediately used to calculate the contour integrals in Eqs. (5) and (6), this quadrature is very inefficient when the accuracy is estimated from a comparison of $\tilde{\boldsymbol{\Sigma}}^{pq}(\omega)$ obtained for different numbers of energy points n_z. In order to overcome this difficulty, for the computation of the contour path contribution to $\tilde{\boldsymbol{\Sigma}}^{pq}(\omega)$, the Konrod-Legendre rule was adapted.[25] The basic idea proven by Konrod[37] is that one can determine $2n_z+1$ nodes including all nodes of an n_z-point Gauss quadrature such that each of the additional n_z+1 nodes falls in between two nodes of the n_z-point Gauss quadrature. Because within the Gauss-Legendre rule all n_z nodes are roots of n_zth order Legendre polynomials corresponding to a unity weighting function, the construction of the Jacobi-Konrod matrix is not a trivial task. The present implementation closely follows Laurie's mixed moments algorithm to generate the Jacobi-Konrod matrix for even n_z.[38] The main advantage of the so-performed Konrod quadrature is that having evaluated the integrand for $2n_z+1$ nodes, both the Gauss sum $\mathcal{G}_{n_z}\tilde{\boldsymbol{\Sigma}}^{pq}(\omega)$ and the Konrod sum $\mathcal{K}_{2n_z+1}\tilde{\boldsymbol{\Sigma}}^{pq}(\omega)$ are simulta-

neously available. By comparing these sums on each particular part of the contour, $\tilde{\Sigma}^{pq}_{\mu\nu}(\omega)$ is considered to be converged if the criterion

$$\max|\mathcal{K}_{2n_z+1}\tilde{\Sigma}^{pq}_{\mu\nu}(\omega) - \mathcal{G}_{n_z}\tilde{\Sigma}^{pq}_{\mu\nu}(\omega)| \leqslant \epsilon_z, \tag{A1}$$

is fulfilled for a given ϵ_z defining the accuracy.

APPENDIX B: CUMULATIVE SPECIAL-POINTS METHOD

The special-points method (SPM) is the counterpart of the Gauss quadrature in $\vec{k}$ space. Within the SPM, the integrand is expanded in terms of symmetrized plane waves $A_m(\vec{k})$, which are real and translationally and point-symmetry group rotationally invariant functions orthogonal to each other. Therefore, the special points $\vec{k}_j$ are solutions of the homogeneous system:

$$\sum_{j=1}^{n_k} w_j A_m(\vec{k}_j) = 0 \quad (m = 0,1,\ldots,M), \tag{B1}$$

where the sum of weights $w_j = w(\vec{k}_j)$ considered over all $\vec{k}$ points ($j=1,\ldots,n_{\vec{k}}$; $n_{\vec{k}}$ being the number of special points) equals 1. It has been shown[39] that $\vec{k}$ points of a uniform, periodic mesh,

$$\vec{k}_j = \sum_{\alpha=1}^{d_{\mathrm{BZ}}} k_{j_\alpha}\vec{b}_\alpha,$$

taken with respect to the edges $\vec{b}_\alpha$ of the reciprocal unit cell (d_{BZ} is the dimension of the Brillouin zone, i.e., $d_{\mathrm{BZ}}=2$ or 3), where

$$k_{j_\alpha} = \frac{j_\alpha - 1}{n_\alpha} + \mathsf{a}_\alpha - \frac{1}{2}, \quad j_\alpha = 1,\ldots,n_\alpha, \tag{B2}$$

are solutions of Eq. (B1), minimizing the remainder in the expansion of the integrand. Exploiting the arbitrariness of the parameter a_α in Eq. (B2), the SPM has been extended in Ref. 25 by proving that successively denser $\vec{k}$ meshes including all $\vec{k}$ points of the previous meshes can be created independently on d_{BZ} if and only if a_α does not depend on n_α. According to this statement, the so-developed cumulative special-points method (CSPM) can be viewed in some extent as the analog of the Konrod quadrature in $\vec{k}$ space. In particular, by using $n_i = 2^{i+2}n_0$ ($n_0 \in N$) divisions along each $\vec{b}_\alpha$, with $\alpha=1,\ldots,d_{\mathrm{BZ}}$, in the two-dimensional $\vec{k}$ space ($d_{\mathrm{BZ}}=2$), the CSPM permits all $\vec{k}$-space integrations to be performed with an arbitrary high precision $\epsilon_{\vec{k}}$ by applying the convergence criterion:

$$\max|\mathcal{S}_{n_i}\tilde{\Sigma}^{pq}_{\mu\nu}(z \pm \hbar\omega + i\delta, z) - \mathcal{S}_{n_{i-1}}\tilde{\Sigma}^{pq}_{\mu\nu}(z \pm \hbar\omega + i\delta, z)| \leqslant \epsilon_{\vec{k}}, \tag{B3}$$

for each complex energy point on the contour and Matsubara pole, respectively. Note that here all optical conductivity tensor calculations were carried out such that the convergence criteria (A1) and (B3) were fulfilled for $\epsilon_z = \epsilon_{\vec{k}} \leqslant 10^{-3}$ a.u.

[1] C. S. Tian, D. Qian, D. Wu, R. H. He, Y. Z. Wu, W. X. Tang, L. F. Yin, Y. S. Shi, G. S. Dong, X. F. Jin, X. M. Jiang, F. Q. Liu, H. J. Qian, K. Sun, L. M. Wang, G. Rossi, Z. Q. Qiu, and J. Shi, Phys. Rev. Lett. **94**, 137210 (2005).

[2] R. Mattheis and G. Quednau, Phys. Status Solidi A **172**, R7 (1999); J. Magn. Magn. Mater. **205**, 143 (1999).

[3] I. Reichl, A. Vernes, P. Weinberger, L. Szunyogh, and C. Sommers, Phys. Rev. B **71**, 214416 (2005).

[4] J. Zabloudil, R. Hammerling, L. Szunyogh, and P. Weinberger, *Electron Scattering in Solid Matter: A Theoretical and Computational Treatise*, Springer Series in Solid-State Sciences (Springer Verlag, Berlin, 2005).

[5] R. Kubo, J. Phys. Soc. Jpn. **12**, 570 (1957).

[6] R. Kubo, M. Toda, and N. Hashitsume, *Statistical Physics II: Nonequilibrium Statistical Mechanics* (Springer-Verlag, Berlin, 1985).

[7] J. M. Luttinger, in *Mathematical Methods in Solid State and Superfluid Theory*, edited by R. C. Clark and G. H. Derrick, Proceedings of the Scottish Universities' Summer School 1967 (Oliver and Boyd, Edinburgh, 1969), Chap. 4, p. 157.

[8] A. Vernes, L. Szunyogh, and P. Weinberger, Phase Transitions **75**, 167 (2002).

[9] P. Weinberger, *Electron Scattering Theory for Ordered and Disordered Matter* (Oxford University Press, Oxford, 1990).

[10] L. Szunyogh and P. Weinberger, J. Phys.: Condens. Matter **11**, 10451 (1999).

[11] P. Weinberger, P. M. Levy, J. Banhart, L. Szunyogh, and B. Újfalussy, J. Phys.: Condens. Matter **8**, 7677 (1996).

[12] F. Abelés, Ann. Phys. (Paris) **5**, 596 (1950).

[13] D. O. Smith, Opt. Acta **12**, 13 (1965); R. P. Hunt, J. Appl. Phys. **38**, 1652 (1967).

[14] P. Yeh, Surf. Sci. **96**, 41 (1980); J. Zak, E. R. Moog, C. Liu, and S. D. Bader, J. Magn. Magn. Mater. **89**, 107 (1990); R. Atkinson and P. H. Lissberger, *ibid.* **118**, 271 (1993).

[15] A. Vernes, Philos. Mag. **86**, 1973 (2006).

[16] M. Mansuripur, J. Appl. Phys. **67**, 6466 (1990); *The Principles of Magneto-Optical Recording* (Cambridge University Press, Cambridge, England, 1995).

[17] A. Vernes, L. Szunyogh, L. Udvardi, and P. Weinberger, J. Magn. Magn. Mater. **240**, 215 (2002).

[18] L. D. Landau and E. M. Lifshitz, *Electrodynamics of Continuous Media*, Course of Theoretical Physics Vol. 8 (Butterworth-Heinemann, Oxford, 1999).

[19] A. K. Zvezdin and V. A. Kotov, *Modern Magnetooptics and Magnetooptical Materials, Studies in Condensed Matter Physics* (Institute of Physics, Bristol, 1997).

[20] J. D. Jackson, *Classical Electrodynamics* (Wiley, New York, 1975).
[21] A. Vernes, L. Szunyogh, and P. Weinberger, Phys. Rev. B **65**, 144448 (2002).
[22] A. Vernes, I. Reichl, P. Weinberger, L. Szunyogh, and C. Sommers, Phys. Rev. B **70**, 195407 (2004).
[23] A. Vernes and P. Weinberger, Phys. Rev. B **70**, 134411 (2004).
[24] R. M. A. Azzam and N. M. Bashara, *Ellipsometry and Polarized Light* (North-Holland, Amsterdam, 1999).
[25] A. Vernes, L. Szunyogh, and P. Weinberger, J. Phys.: Condens. Matter **13**, 1529 (2001).
[26] S. Khmelevskyi and P. Mohn, Phys. Rev. B **75**, 012411 (2007).
[27] S. H. Vosko, L. Wilk, and M. Nusair, Can. J. Phys. **58**, 1200 (1980).
[28] H. J. F. Jansen, Phys. Rev. B **59**, 4699 (1999).
[29] A. Vernes, L. Szunyogh, and P. Weinberger, Phys. Rev. B **66**, 214404 (2002).
[30] B. Koopmans, Phys. Scr. **T109**, 80 (2004).
[31] W. H. Press, B. P. Flannery, S. A. Teukolsky, and W. T. Vetterling, *Numerical Recipes in Fortran: The Art of Scientific Computing* (Cambridge University Press, Cambridge, England, 1992).
[32] A. Hubert and R. Schäfer, *Magnetic Domains* (Springer, Berlin, 1998).
[33] G. Y. Guo and H. H. Wang, Chin. J. Phys. (Taipei) **38**, 949 (2000).
[34] M. S. S. Brooks, Physica B **130**, 6 (1985).
[35] J. Trygg, B. Johansson, O. Eriksson, and J. M. Wills, Phys. Rev. Lett. **75**, 2871 (1995).
[36] H. Ebert and M. Battocletti, Solid State Commun. **98**, 785 (1996).
[37] A. S. Konrod, *Nodes and Weights of Quadrature Formulas* (Consultants Bureau, New York, 1965).
[38] D. P. Laurie, Math. Comput. **66**, 1133 (1997).
[39] J. Hama and M. Watanabe, J. Phys.: Condens. Matter **4**, 4583 (1992).